Dynamic morphogenesis of a pioneer axon in *Drosophila* and its regulation by Abl tyrosine kinase

Akanni Clarke[a,b], Philip G. McQueen[c], Hsiao Yu Fang[a], Ramakrishnan Kannan[a,†], Victor Wang[c,‡], Evan McCreedy[c], Tyler Buckley[a,§], Erika Johannessen[a,||], Stephen Wincovitch[d], and Edward Giniger[a,*]

[a]National Institute of Neurological Disorders and Stroke, [c]Center for Information Technology, and [d]National Human Genome Research Institute, National Institutes of Health, Bethesda, MD 20892; [b]Department of Biochemistry and Molecular Medicine, George Washington University School of Medicine/NIH Graduate Partnership Program, Washington, DC 20037

ABSTRACT The fundamental problem in axon growth and guidance is to understand how cytoplasmic signaling modulates the cytoskeleton to produce directed growth cone motility. We here dissect this process using live imaging of the TSM1 axon of the developing *Drosophila* wing. We find that the growth cone is almost purely filopodial, and that it extends by a protrusive mode of growth. Quantitative analysis reveals two separate groups of growth cone properties that together account for growth cone structure and dynamics. The core morphological features of the growth cone are strongly correlated with one another and define two discrete morphs. Genetic manipulation of a critical mediator of axon guidance signaling, Abelson (Abl) tyrosine kinase, shows that while Abl weakly modulates the ratio of the two morphs it does not greatly change their properties. Rather, Abl primarily regulates the second group of properties, which report the organization and distribution of actin in the growth cone and are coupled to growth cone velocity. Other experiments dissect the nature of that regulation of actin organization and how it controls the spatial localization of filopodial dynamics and thus axon extension. Together, these observations suggest a novel, probabilistic mechanism by which Abl biases the stochastic fluctuations of growth cone actin to direct axon growth and guidance.

INTRODUCTION

The process of axon guidance is central to patterning the nervous system during development. Understanding how axons pathfind to their correct targets requires that we know the mechanism by which guidance information in the environment controls the spatial organization and dynamics of the growth cone cytoskeleton to produce directed extension of the axon. It is widely accepted that in some cases broad, flat, growth cones extend the axon by harnessing the adhesive properties of large lamellipodia (Lewis and Bridgman, 1992; Lin and Forscher, 1995). There is reason to suspect, however, that other axons pathfind and extend in an entirely different way.

Cells in culture can switch mechanisms of cell motility depending on the developmental context. For example, fibroblasts make large lamellipodia in 2D culture, yet assume spindle-shaped morphologies and move faster in 3D environments (Cukierman *et al.*, 2001). Mesenchymal cells use a slow-moving, adhesive style of growth in 2D culture, but switch to a fast, ameboid style of growth in 3D conditions of low adhesion and strong confinement (Liu *et al.*, 2015).

Dendritic cells rely on integrins for 2D cell migration, but 3D migration in vivo is protrusive and independent of integrin function (Lammermann et al., 2008). These examples demonstrate that the molecular components and mechanisms used by diverse cell types to move in 2D versus 3D environments are consistently and fundamentally different.

Much as cell motility can be accomplished in multiple ways, there is also evidence for a second mode of axon growth. It has been reported that filopodial protrusions alone can extend some axons. In these cases, it seems that rather than applying adhesive traction to lamellipodia to pull the growth cone forward, axon growth is instead accomplished by selective stabilization and dilation of individual filopodia (O'Connor et al., 1990; Sabry et al., 1991). This filopodial style of growth has been proposed as a common mechanism for axon growth (O'Connor et al., 1990; Grabham et al., 2003), but it is not clear how such a mechanism would work, or how signaling molecules would regulate it.

To understand how signaling controls axon growth and guidance, there has been a sustained effort to find and characterize individual molecules that are linked to fundamental steps in the mechanism of axon extension and guidance. One such protein, the Abelson (Abl) nonreceptor tyrosine kinase, acts downstream of nearly all of the common, phylogenetically conserved families of axon guidance receptors (Wills et al., 1999; Bashaw et al., 2000; Yu et al., 2001; Crowner et al., 2003; Forsthoefel et al., 2005; Dajas-Bailador et al., 2008). Abl is critical for axon patterning (Koleske et al., 1998; Grevengoed et al., 2001, 2003; Liebl et al., 2003; Moresco and Koleske, 2003) and acts in cooperation with a cohort of accessory factors that regulate the organization and dynamics of the actin cytoskeleton including Enabled/VASP, Disabled, Abi, Trio, Rac, and WAVE, among others (Grevengoed et al., 2003; Song et al., 2010). We have recently demonstrated that one key function of Abl signaling in axons is to balance linear extension of actin filaments with actin branching, through its ability to suppress the activity of a linear actin polymerizing factor (Enabled), and simultaneously stimulate an actin branching mechanism (WAVE/Scar and Arp 2,3 under control of Trio and Rac) (Kannan et al., 2017). These roles place Abl at the key interface between extracellular signaling and intracellular modulation of the axonal cytoskeleton, though it remains unclear how these molecular interactions execute the cellular function of axon growth and guidance.

We therefore set out to use live imaging of a single pioneer neuron in its native environment to understand how a pathfinding axon extends and how Abl controls it. Here we present methods to image and computationally quantify both the neuronal morphology and the cytoskeletal dynamics of the TSM1 axon as it extends along its native trajectory in the intact Drosophila wing. Using these data, in the current paper we focus on defining the dynamic morphology of that axon and querying growth cone properties to determine how they interact and which are targets of Abl-dependent signaling. We show that the TSM1 growth cone is almost purely filopodial in morphology, that it advances by a protrusive mode of growth, and that it contains an accumulated mass of actin in the distal axon that is closely associated with the dynamic filopodial domain that morphologically defines the growth cone. Quantification of the defining features of the growth cone reveals that they fall into two separate clusters of properties, each of which is highly correlated internally, though the two clusters are largely independent of each other. The core morphological parameters of the growth cone are strongly correlated with one another, defining two highly branched morphs that, while similar, are qualitatively distinct, and axons can transition between the two morphs as they extend. Gain- and loss-of-function of

Abl tyrosine kinase reveals that while it weakly modulates the relative occupancy of the two morphs, it does not materially alter the properties of either one. Rather, the overwhelming effect of Abl is to regulate the second cluster, which comprises parameters reporting the distribution and organization of actin in the growth cone, and which is, in turn, correlated with instantaneous growth cone velocity. In the accompanying paper (Clarke et al., 2020), we will turn to a more detailed analysis of the nature of that actin organization and dissect how it controls the spatial distribution of growth cone dynamics and thereby directs growth cone motility.

RESULTS

Live imaging of the TSM1 pioneer axon in its native tissue

In light of the historical difficulty in observing cytoskeletal dynamics in growing axons in vivo (Dent and Gertler, 2003), we developed such a system by exploiting a pioneer sensory neuron of the Drosophila wing, called TSM1. During metamorphosis, the TSM1 axon extends in the space between the dorsal and ventral epithelia of the wing, pioneering the growth of the L1 nerve laterally from the wing margin before turning and extending proximally toward the wing hinge. The axon extends approximately 120 μm over a 9- to 12-h period along this trajectory before it fasciculates with the L3 nerve at the L1–L3 junction just distal to the GSR neuron (Murray et al., 1984) (Figure 1, A and B). It has been shown previously that axons in cultured wing disk explants are robust and pathfind faithfully (Blair and Palka, 1985). Furthermore, the wing anatomy allows for an unobstructed view of TSM1 development. Therefore, TSM1 provides an excellent opportunity to observe axonal growth and guidance in detail as the growth cone pathfinds through its native environment.

We live-imaged TSM1 axon extension in explanted early pupal wing imaginal discs by spinning disk confocal microscopy, with simultaneous visualization of the axonal membrane, using neuron-specific expression of CD4 Tandem-Tomato, and intracellular actin using Lifeact-GFP (which labels both F- and G-actin; Riedl et al., 2008). Reporter expression was driven with neuralized-GAL4, which is a pan-neural GAL4 line that comes on early in neuronal differentiation. Z-stacks were collected every 3 min for 1.5 h from 14 trajectories of wild type and of flies with altered levels of Abl tyrosine kinase: Abl knockdown (KD) and Abl overexpression (OE). Both altered-Abl conditions were induced using UAS-driven Abl-modulatory constructs under control of the same, neuronal-specific GAL4 used for reporter expression. Axon morphology was traced stereoscopically in 3D, and the intensity of the Lifeact-GFP signal was quantified along the axon shaft from the base of the axon to its distal tip. We focus on actin organization both because of its well-established, critical role in cell and growth cone motility and because it is the best characterized downstream target of Abl signaling. Control experiments showed that imaging of developing transgenic wings in culture does not disturb the trajectory of the axon, or the ability of these axons to reach the L1–L3 junction and fasciculate with the L3 nerve.

Live imaging revealed that TSM1 has a defined domain of filopodial protrusiveness in the distal portion of the axon, and that this domain advances along the genetically specified trajectory of the definitive axon (Figure 1C and Supplemental Video S1). The filopodial domain is a branched, 3D structure, as highly extended in the z-axis as it is in the x- and y-axes (Figure 2A). In all imaged time points, filopodia and transient axonal branches (referred to collectively as protrusions) were the dominant morphological features of the axon. Large lamellipodia were seen only very rarely (<1% of time points). The pattern of advance was extremely variable, with
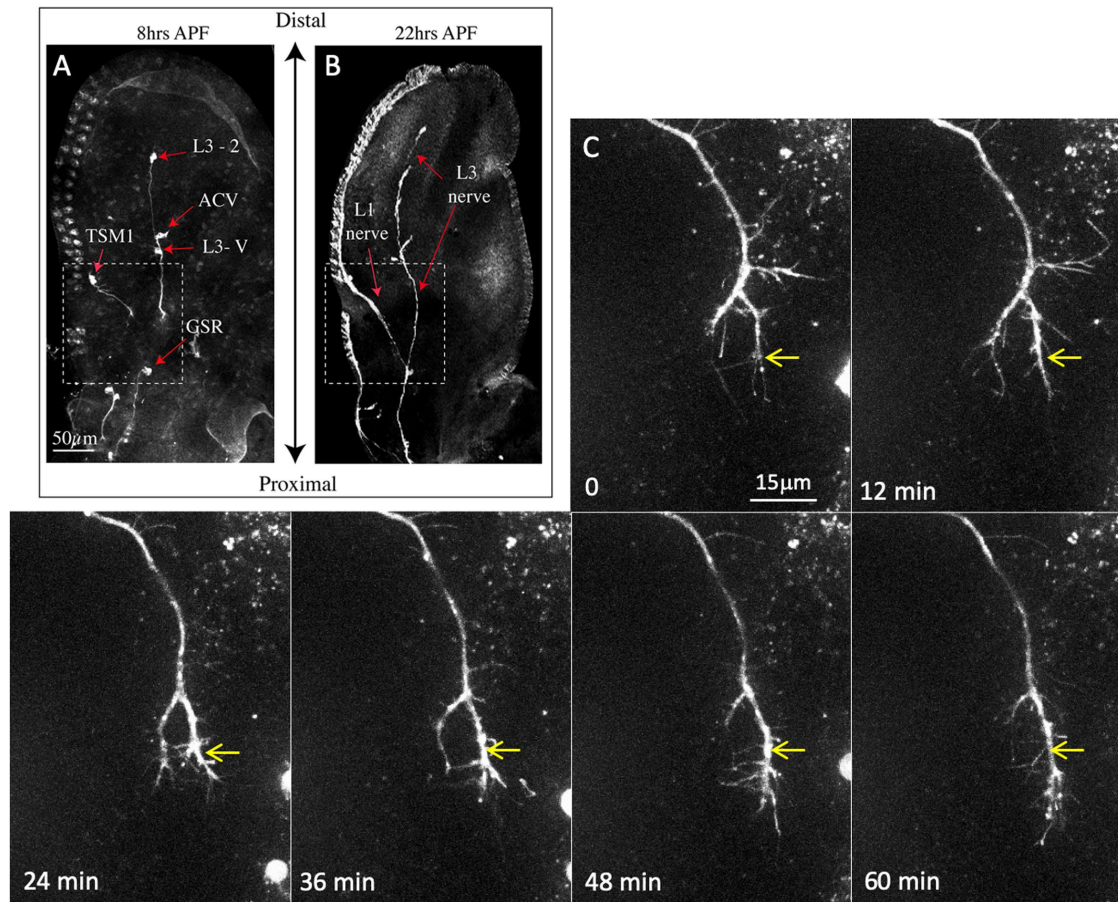
FIGURE 1: Anatomy of TSM1 and filopodial nature of its morphology. Early prepupal wing imaginal discs at different developmental stages were immunostained either for (A) the neuronal membrane (anti-HRP) in 8 h APF discs or (B) microtubules (mAb22C10) in 22 h APF discs and photographed at 10× magnification. TSM1 and the L1 nerve, as well as GSR and other neurons comprising the developing L3 nerve, are highlighted. The box indicates the approximate region that was monitored during video imaging. (C) Gallery of frames from a video showing TSM1 growth cone during a single trajectory (wild-type cell 5). Only td-Tomato (membrane) channel is shown for clarity. Times of individual frames are indicated at the bottom; yellow arrow marks a fixed point in space to allow comparison of net change in axon length.

protrusions extended equivalently along both the preferred final direction of growth and along nonpreferred directions. Transient branches extending in nonpreferred directions were capable of becoming large and engorged and sometimes persisted for many time points before being retracted.

The TSM1 growth cone has a core of accumulated actin that advances together with the domain of protrusive dynamics

In concert with the protrusive domain of the distal axon, we invariably observed a local accumulation of high actin intensity (Figure 2, B–D, and Supplemental Figure S1), and this accumulation of actin advanced as the axon extended (Figure 2F; for clarity, the individual actin profiles of the time points comprising Figure 2F are presented as a gallery in Supplemental Figure S2, and the complete associated video is Supplemental Video 2). To track the position and dynamics of this actin mass, we developed computational tools to quantify the profile of actin intensity along the length of the axon (see *Materials and Methods*). Throughout this manuscript, we refer to the curve that reports the relative actin intensity as a function of position along the axon as the "actin distribution" (see, for example, Figure 2D). Note that confocal imaging methods can only resolve this bulk actin distribution, which incorporates actin transport, diffusion, polymer-

ization/de-polymerization, etc.; they cannot resolve the motions of individual actin molecules. Actin accumulation in the distal axon was also observed using other actin markers, including F-tractin Tandem-tomato, which selectively labels F-actin, whereas a volume marker (cytoplasmic eGFP) showed little or no distal accumulation (Supplemental Figure S3, A and B, respectively). Time-lapse image sequences suggested that the mass of accumulated actin and the zone of enhanced protrusion density advanced in concert as the axon grew (Supplemental Video S2). To assess quantitatively the relationship between accumulated actin and protrusion density along the axon, we first performed a sliding window analysis to determine the position of the maximum value for each of these properties, separately, along the TSM1 axon in each image. Quantification confirmed that the interval with the highest actin level (actin maximum) and the interval with the highest protrusion density (protrusion maximum) were strongly correlated in position along the axon, (Pearson $r = 0.71$; $p < 0.0001$) (Figure 2G), and this held true across a range of window sizes (range 1–10 μm). Furthermore, the correlation of actin intensity values with local protrusion count was not restricted to the distal coconcentration of actin and protrusions. Global comparison affirmed the relationship between actin intensity and local protrusion count along the entire axon (Pearson r correlation = 0.60;
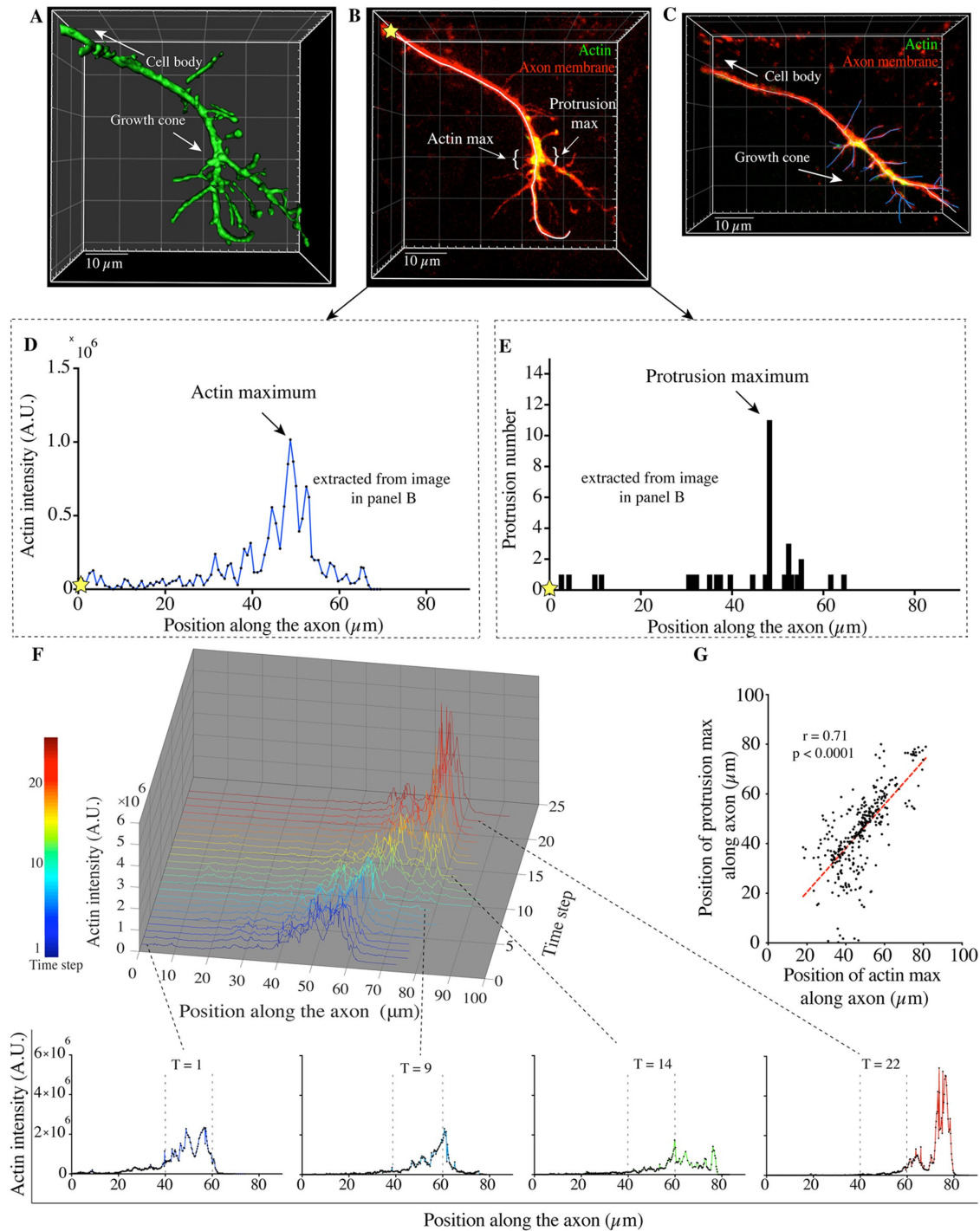
FIGURE 2: The TSM1 growth cone accumulates actin and is dominated by filopodial protrusions. The TSM1 axon was imaged in the intact wing. Image stacks were segmented and actin intensity was quantified along the axon shaft. (A) Three-dimensional rendering of the cell membrane and (B) z-projected image of the distal axon of TSM1 from one typical video frame from wild type. In B, membrane is in red, actin is in green, and the axon shaft has been traced in white. (See Supplemental Figure S1 for unmerged color channels and pseudocolored actin channel.) (C) A fully segmented image of the distal TSM1 axon: protrusions are traced in blue and the axon shaft is traced in white. (D) A representative actin distribution extracted from the lifeact-GFP signal of the axon in B. The yellow star demarcates the origin of the actin profile. (E) A representative distribution of protrusions extracted from the traced axonal membrane channel of the axon in B. The yellow star demarcates the origin of the tracing. (F) A three-dimensional plot of sequential actin profiles extracted over time from a single TSM1 trajectory. Profiles were extracted from images captured every 3 min. Actin distributions from four individual time points are shown separated below to highlight actin advance by "inchworming" (see accompanying paper [Clarke *et al.*, 2020] for further discussion of this phenomenon); actin profiles of all individual time points are also presented as a gallery of images in Supplemental Figure S2. (G) Scatter plot of the positions of maximum protrusion density vs. maximum actin intensity along the axon; $n = 338$ time points from 14 individual trajectories; *r* is Pearson correlation; *p* is by paired *t* test.

Abl shapes growth cone morphogenesis |

$p < 0.0001$). This relationship was also consistent when we compared the lengths of protrusions, rather than the count, with the distribution of actin intensity (Pearson r correlation = 0.45; $p < 0.0001$). These data demonstrate that the length and number of axonal protrusions at particular positions along the axon shaft are strongly correlated to the local amount of accumulated actin.
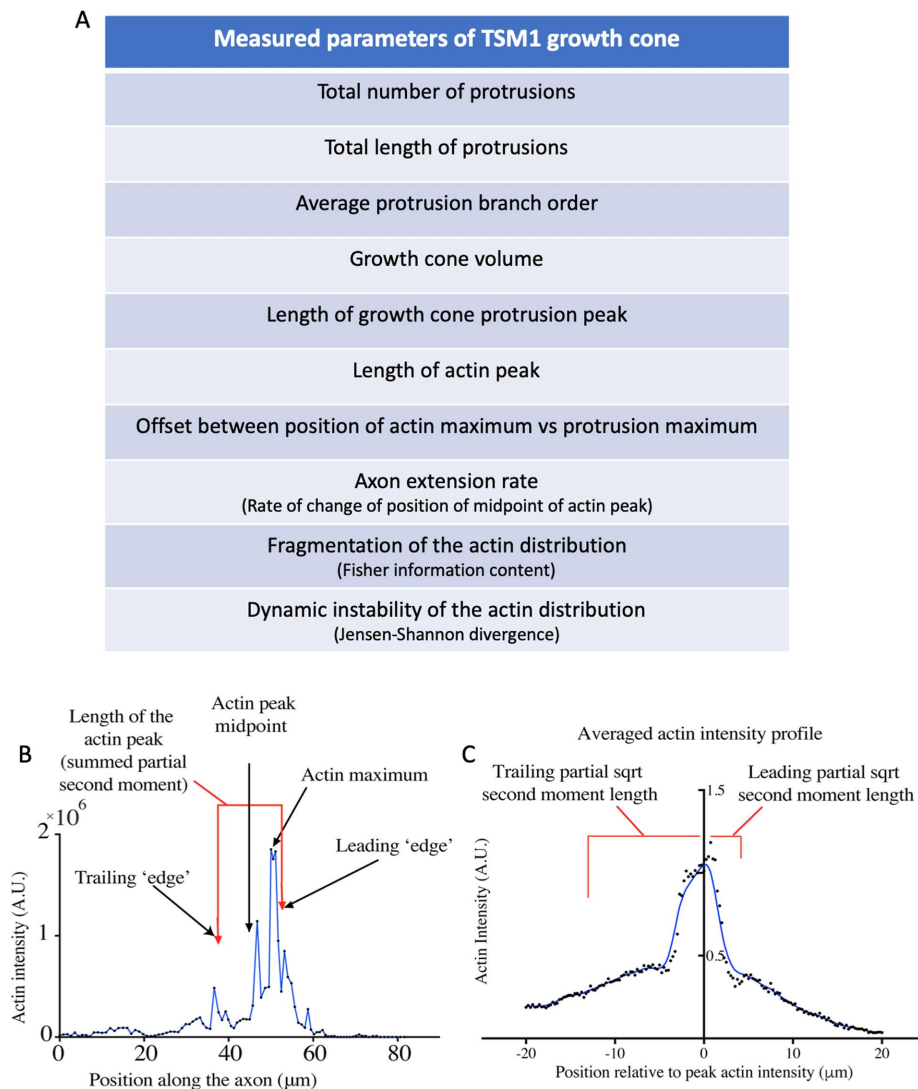
Abl tyrosine kinase regulates TSM1 axon patterning

To validate a powerful, and physiologically relevant, reagent for interrogating the mechanism of TSM1 growth cone dynamics, we verified that the Abl tyrosine kinase is required for growth and guidance of TSM1, just as it is required for many other axons in the CNS and PNS of *Drosophila* and of vertebrates (Wills *et al.*, 1999; Bashaw *et al.*, 2000; Crowner *et al.*, 2003; Forsthoefel *et al.*, 2005). We found that perturbing Abl activity or expression caused aberrant TSM1 axon growth and guidance phenotypes, including instances where axonal growth stalled (Figure 3B), no axon extended from the cell body (Figure 3C), the axon misrouted along its trajectory (Figure 3D), and/or the axon maintained aberrant collateral branches (Figure 3B). Specifically, reducing Abl expression by RNA interference (RNAi) in the background of Dicer 2 OE (Abl KD) caused an increase in aberrant TSM1 axon growth and guidance phenotypes (UAS-Abl RNAi, 51% vs. control 11%; $p < 0.0001$, Figure 3E). The expressivity of TSM1 axon defects observed in Abl KD was enhanced by heterozygosity for an Abl mutant allele (83% with UAS-Abl RNAi/Abl[4] vs. UAS-Abl RNAi, 50%; $p = 0.002$, Figure 3E), confirming the fidelity of the RNAi phenotype. Expression of Dicer2 alone also increased the frequency of subtle defects in TSM1 morphology (32% vs. 11% in control, Figure 3E), but the spectrum of defects is significantly different from and less severe than that in the presence of Abl RNAi ($p = 0.0035$, χ^2, Supplemental Figure S4; also see Supplemental Figure S4 for quantification of the pattern of defects in all key experimental conditions), and OE of Dicer 2 alone did not affect cytoskeletal parameters measured in growing axons. To discriminate the catalytic function of Abl kinase from its scaffolding role, we treated wings with Imatinib, a specific small molecule inhibitor of Abl kinase activity, and found significant TSM1 axonal defects when compared with control (61% in 10 µM Imatinib vs. control 11%; $p < 0.0001$, Figure 3E). This result strongly suggests that kinase activity is critical, though it does not exclude an important function for scaffolding. We also observed axonal defects when Abl was overexpressed (Abl OE 35% vs. control 11%; $p = 0.0123$, Figure 3E). Taken together, these results demonstrate that precise tuning of Abl function is required for TSM1 axon extension and guidance.
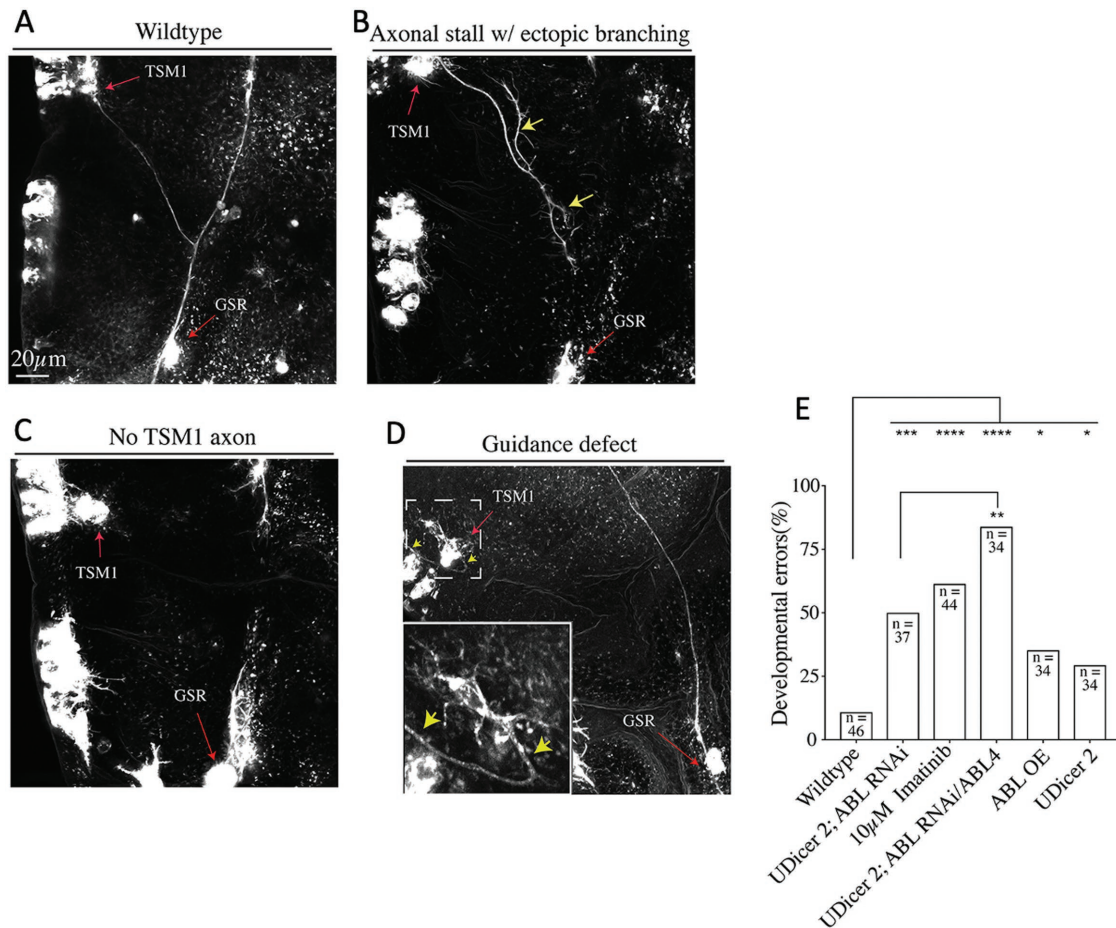
FIGURE 3: Abl regulates TSM1 axon guidance and extension. Prepupal wing imaginal discs expressing td-Tomato in neurons (*neur-GAL4*) were allowed to develop in culture to the completion of TSM1 axon extension (~24 h APF) and imaged by confocal microscopy. (A–D) 25× micrographs of terminal TSM1 axon phenotypes. (A) Wild-type TSM1 developmental pattern and (B–D) examples of observed developmental errors. Yellow arrows in B and D highlight aberrant TSM1 axonal phenotypes. Red arrows highlight TSM1 and GSR. The specific phenotypes depicted were not restricted to the specific genotypes used for illustration. (B) *neur-GAL4; UDicer2; Abl RNAi/Abl[4]*, (C, D) *neur-GAL4; UDicer2; Abl RNAi*. (E) Histogram plotting the frequency of terminal TSM1 developmental errors in the indicated genotypes. *$P < 0.05$, **$P < 0.01$, ***$P < 0.005$, ****$P < 0.0001$; Fisher's exact T test.

A

Measured parameters of TSM1 growth cone
Total number of protrusions
Total length of protrusions
Average protrusion branch order
Growth cone volume
Length of growth cone protrusion peak
Length of actin peak
Offset between position of actin maximum vs protrusion maximum
Axon extension rate (Rate of change of position of midpoint of actin peak)
Fragmentation of the actin distribution (Fisher information content)
Dynamic instability of the actin distribution (Jensen-Shannon divergence)

FIGURE 4: Measured properties of the TSM1 axon. (A) Listing of the parameters included in the analyses presented here. See text and *Materials and Methods* for detailed descriptions of these parameters and their definitions. (B) Attributes of a representative actin distribution are annotated to demarcate the length, the maximum, and the midpoint of the actin peak, as well as the nominal leading and trailing boundaries of the distribution (the leading and trailing square root of the second moment of the distribution, respectively; see *Materials and Methods*). (C) Average actin intensity profile: 338 individual actin profiles were aligned by the actin intensity maximum and averaged. The average leading and trailing partial sqrt(second moment) about the aligned actin maximum are indicated.

Development of metrics to quantify TSM1 morphology and actin organization

To dissect quantitatively the morphology and dynamics of the TSM1 growth cone, we developed a robust and comprehensive set of parameters that could be measured objectively and that captured the properties of the developing axon. We investigated more than 40 candidates for static and dynamic measures before reducing them to a set of 10 that subsumed all of the significant features we could identify visually and that could be quantified by a user-independent computational pipeline (Figure 4A; see also *Materials and Methods*). In brief, this included measures of the branching properties of the axon, for example, branch number, branch length, branch order, the length of the filopodial domain of the growth cone, and the volume

of space surveyed by the growth cone filopodia (referred to as growth cone volume). We also developed measures of actin organization, including the length of the actin mass associated with the growth cone, the speed of its advance, and measures of its degree of internal organization (i.e., coherence) both statically (Fisher Information Content [FI], which reports the degree of fragmentation of the actin distribution at each individual time point) and dynamically (Jensen–Shannon divergence [JSD], which reports the overlap of the distribution between two time points, i.e., how well the shape of the distribution at one time point predicts its shape at the next). Below, we refer to the static measure of coherence at each individual time point as the "actin fragmentation" and the dynamic measure between each pair of time points as the "dynamic instability of the actin distribution"; see *Materials and Methods* for detailed definitions. We point out that while in individual time points the stochastic dynamics of actin may transiently give the impression of the leading actin mass fragmenting into more or less separated elements (Figure 4B), quantitative analysis of the dataset as a whole makes it clear that the mass of growth cone actin is best treated as a single entity, which we call the "actin peak" (Figure 4C). Below we investigate these parameters and their modulation by Abl systematically, first as single parameters, then in pairwise combinations, and finally by a global principal components analysis.

Abl modestly modulates individual morphological properties of the TSM1 growth cone

Modulating Abl activity had modest, but statistically significant, effects on a number of the branching properties of TSM1. For example, either loss- or gain-of-function of Abl led to an increase in both the number and the length of protrusions emanating from the growth cone (Figure 5, A and B). In contrast, reducing versus increasing Abl level had opposite effects on the length of the protrusion peak, with Abl KD decreasing its length (14.5 µm ± 0.18 in Abl KD vs. 15.9 µm ± 0.21 in control; $p < 0.05$) and Abl OE increasing it (18.9 µm ± 0.27; $p < 0.001$; Figure 5C). Similarly, the length of the actin peak is also decreased in the Abl KD condition, but increased by Abl OE (15.16 µm ± 0.19 in control vs. 14.0 µm ± 0.27 in KD; $p = 0.0051$, and 16.72 µm ± 0.32 in OE; $p = 0.0002$; one-way analysis of variance [ANOVA], Figure 5D; in Dicer 2 alone, actin peak length = 15.83 µm ± 0.24; not significant vs. control). Although all the differences described above are statistically significant, their biological significance was not immediately obvious. For example, these changes apparently do not have a large impact on the average growth rate of the axon, which is not significantly altered in Abl KD or Abl OE (WT = 0.23 ± 0.05 mm/min vs. Abl KD = 0.19 ± 0.08 and Abl OE = 0.26 ± 0.07; differences not significant: ANOVA).
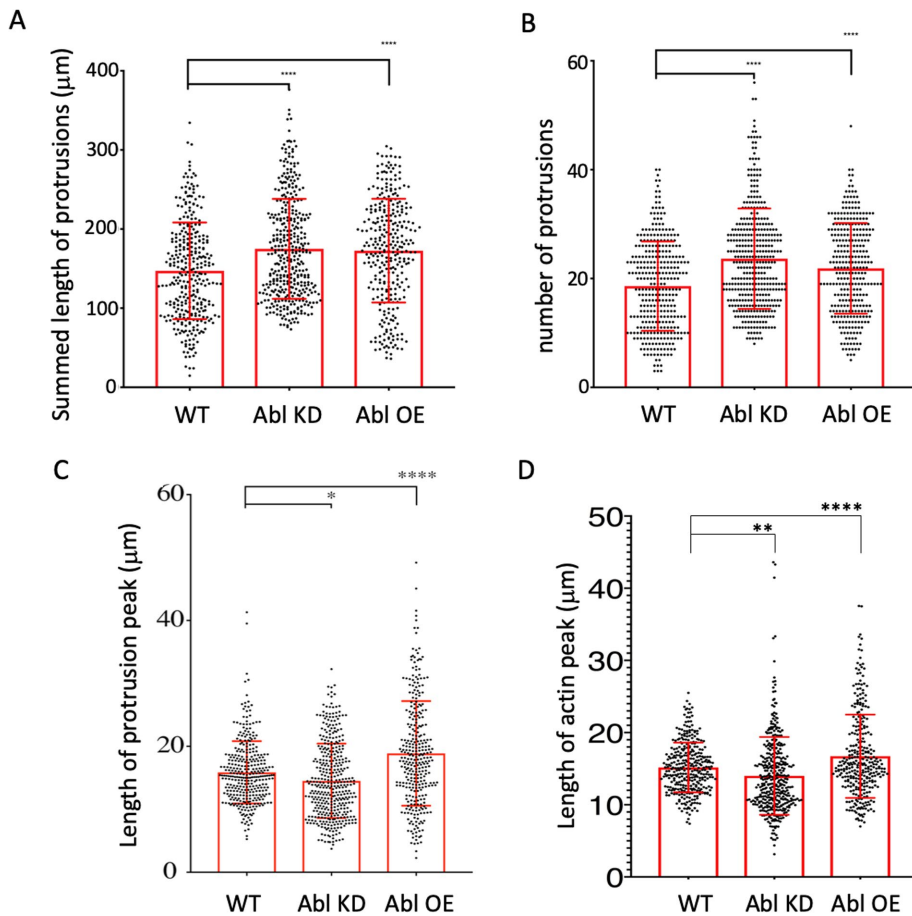
FIGURE 5: Altering Abl level modifies aspects of morphology and actin organization The indicated parameters were measured in all time points of videos of wings from wild-type control, Abl KD, and Abl OE. Red bars show mean values; whiskers indicate SD. Significance (ANOVA, corrected for multiple testing) indicated by black lines is as follows: *$p < 0.05$; **$p < 0.01$; ****$p < 0.0001$. (A) Total protrusion length. (B) Total protrusion number. (C) Length of protrusion peak. (D) Length of actin peak.

Pairwise correlations of parameters reveal two separate clusters of highly correlated features of the growth cone

Investigation of the pairwise correlations among the parameters that characterize TSM1 revealed two clusters of features in the growth cone, each of which comprised a network of highly correlated parameters, though the two networks were largely uncorrelated with each other. We quantified by Pearson correlation all of the pairwise correlations of the 10 parameters we defined for TSM1 (Figure 6A). Operationally, we found that accepting as significant a cutoff of $r = 0.2$ (or –0.2) was effective for identifying correlations that were significant based on Kendall tau analysis, where the criterion for significance was taken as requiring *both* $p < 0.05$ after modified Bonferroni correction *and* Benjamini-Hochberg false discovery rate (FDR) < 5%; see *Materials and Methods* (for complete tables of r values, see Supplemental Figure S5; for tau and p values, see Supplemental Figure S6, A and B, respectively).

Examining the correlation matrix revealed a cluster of four morphological features that were strongly correlated in nearly all pairwise combinations, and this held true in all three genotypes: wild type, Abl KD, and Abl OE (17/18 correlations pass selection; Figure 6B). These were the branch number, branch length, branch order, and growth cone volume. Evidently, these features are constrained to covary in all TSM1 growth cones, either because of feedbacks among the mecha-

nisms that regulate each of these properties or because they have a common source in the cell biology that gives rise to all them.

Further examination of the matrix revealed a second cluster of correlations. This cluster comprised the two measures of actin coherence—actin fragmentation (assayed by FI) and dynamic instability of actin (assayed by the JSD)—as well as the spatial offset between the positions of the maxima of the actin and projection distributions. This cluster, in turn, was consistently correlated with the instantaneous velocity of the growth cone. As with the morphological cluster, these correlations were found to be significant in almost all comparisons in all three genotypes (11/12 comparisons; Figure 6C).

Global analysis by PCA reveals that the predominant effect of Abl is to modulate actin organization, not branching morphology

To better understand the significance of the two parameter clusters in the correlation matrix, and in particular their relationship to Abl-dependent signaling, we proceeded to interrogate the pattern of interactions globally, by principal component analysis (PCA; see *Materials and Methods* for details). We found, first, that the morphological cluster defined two similar, but distinguishable, branching morphs of TSM1, with individual growth cones capable of transitioning between them, but that Abl had only limited effects on these features. Second, we found, in contrast, that the actin-associated cluster, which is also linked to instantaneous growth cone velocity, was profoundly sensitive to Abl activity.
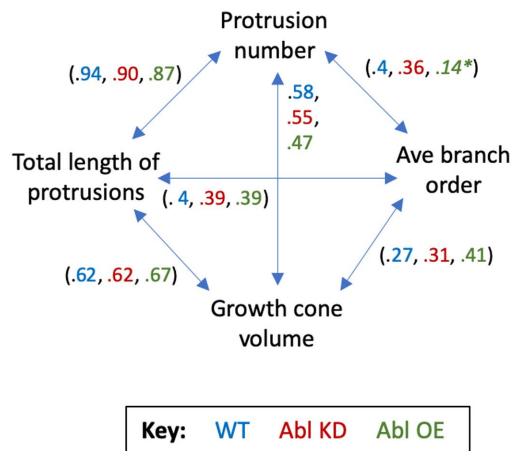
Examination of the first four principal components of the wild-type data set, accounting for ~70% of the total variance, revealed a seemingly homogeneous cloud of component values (Figure 7A). However, on coding the data by trajectory, we observed, first, that each of the 14 cells occupied a restricted portion of the overall parameter space, that is, each was more self-similar than it was similar to the values from any other cell (73/75 pairwise comparisons among these trajectories that have enough data-points for analysis do not satisfy FDR <0.05 (Benjamini-Hochberg FDR; Figure 7, B and C). Second, we observed that the data-points separated into two groups, with 10 of the trajectories falling cleanly into one group or the other, three showing fairly discrete transitions between the groups (Supplemental Figure S7), and one trajectory showing variable occupancy of both. This was most evident after we performed a rotation of the PCA space to better separate the parameters contributing to each axis (called a "Varimax rotation"—see *Materials and Methods* for a detailed explanation; Kaiser, 1958; Abdi, 2003; Figure 7, A–C). Examination of the eigenvalues of VM2 reveals that the major contributions to it are the four, interlinked parameters that compose the morphological cluster observed in the correlation matrix: branch number, branch length, average branch order, and growth cone volume (Figure 7D; compare Figure 6B. See Supplemental
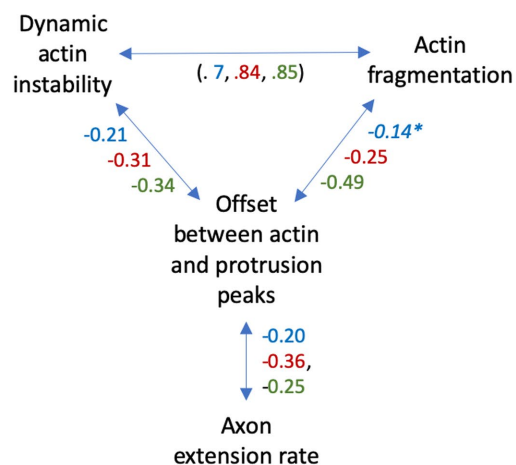
FIGURE 6: Pairwise correlations reveal core properties of the growth cone. Pearson *r* values among the 10 measured parameters were determined for all datapoints for each of the three genotypes (wild type, Abl KD, and Abl OE). (A) Table of correlations. Correlations that passed selection for significance (*r* > 0.2 or < –0.2) are entered in the table and highlighted by colored boxes. Blue boxes indicate comparisons that were significant in all genotypes; green boxes show significance in a subset of genotypes; yellow boxes indicate three cases that are only marginally below the nominal cutoff selected for significance. See Supplemental Figure S5 for a matrix showing all correlation *r* values and Supplemental Figure S6, A and B, for tau- and *p* values, respectively. (B) Inter se correlation values for a cluster of four morphological features that show pairwise significance in 17/18 pairwise combinations. The *r* values are color coded by genotype: wild type, blue; Abl KD, red; Abl OE, green. A single comparison that is below nominal significance is shown with an asterisk and is entered in the table above with the value in green. (C) Correlation *r* values for a cluster of four features having the property that three are correlated inter se (two measures of actin disorder, and the offset between the actin and protrusion maxima; 8/9 comparisons pass selection), while the fourth (axon extension rate) is significantly correlated in all genotypes to the offset measure. Color key is as for B. A single comparison that is below nominal significance is shown with an asterisk and is entered in the table above with the value in blue.

Spreadsheet for quantification). Consistent with this, we see by visual inspection that VM2 (high) growth cones had a relatively simple branching pattern (Figure 7E, top row), while VM2 (low) growth cones were noticeably more complex, with many fine filipodia (Figure 7E bottom row). We did not, however, detect any correlation of this dichotomy with functional features of the trajectory, such as average growth rate (VM2 high = 0.22 ± 0.04 μm/min vs. VM2 low = 0.31 ± 0.05 μm/min; mean ± SEM; difference not significant) or position in the trajectory (e.g., turning regions vs. straight growth).
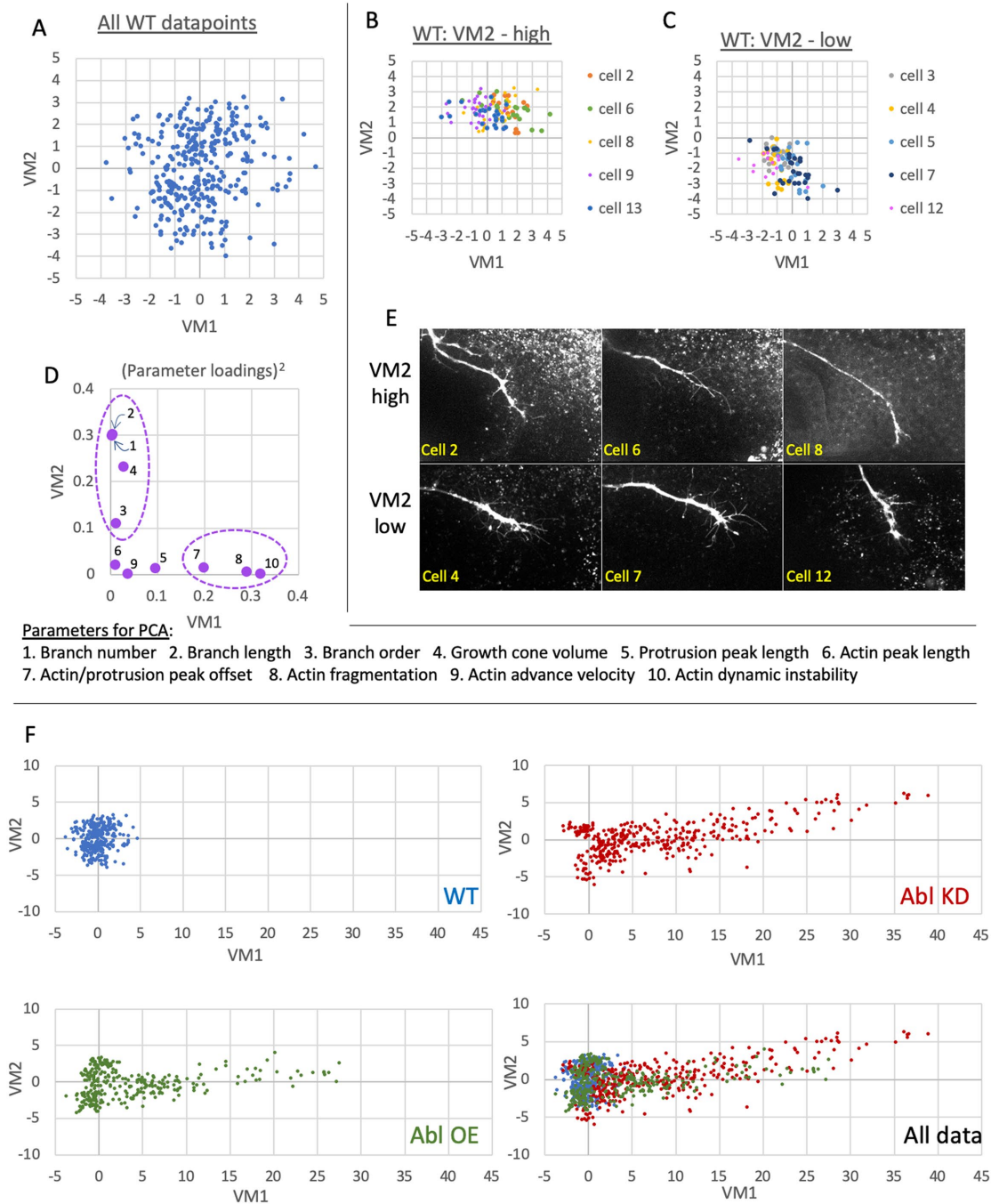
FIGURE 7: Principle component analysis reveals two discrete morphs for TSM1 and shows that Abl selectively regulates actin organization. PCA was performed on the wild-type data set using all 10 parameters. To facilitate analysis and display, the PC1-PC2 plane was rotated such that the contribution of each parameter was assigned optimally to just one of the two coordinate axes (called a Varimax rotation; Kaiser, 1958; Abdi, 2003). To indicate this transformation, the coordinate axes are labeled "VM1" and "VM2," respectively. See text and *Materials and Methods* for a complete description of the Varimax method. (A) Wild-type datapoints displayed in VM1-VM2 space. Note the small gap between a cluster of datapoints above vs. below the *x*-axis. (B) All time points are plotted for the five trajectories that fall entirely within the VM2 > 0 cluster. Individual trajectories are color coded as indicated to highlight the spatial separation between pairs of time points. (C) All time points for the five trajectories that fall entirely within the VM2 ≤ 0 cluster, color coded by trajectory. (D) Plot of (component loading)^2 along VM1 and VM2 for all 10 parameters for WT. Dotted purple ovals indicate the strongest contributions to each axis (loading^2 > 0.1). Individual parameters are identified by numbers, and key to identities is shown below. (E) Single images of growth cone morphology from each of three trajectories in the VM2-high group and the VM2-low group. Each image is labeled with the cell of origin. Note the difference in density of fine protrusions between the two groups. (F) Data from Abl KD and Abl OE were projected on the wild-type VM1-VM2 parameter space. For clarity, the three genotypes are shown separately, and also overlaid. Note that the plot has been extended substantially in the VM1 axis to accommodate the altered-Abl data. Note also that projecting the extended cloud of altered-Abl datapoints back onto the *y*-axis (VM2) reveals that it falls almost entirely within the range of VM2 values observed in wild type.

Next, we projected the Abl KD and Abl OE data onto the wild-type coordinate axes. We found that many of the datapoints from the altered-Abl conditions overlapped the cloud of wild-type data and fell into the same two clusters representing the two growth cone morphs (Figure 7F). However, the remaining data from the genetically altered conditions did not simply spread out isotropically, nor did they populate a distant, separated region of parameter space. Instead, they projected along a narrow, defined vector that emanated from the wild-type cloud of parameter values and extended along the VM1 axis. Examination of the significant contributions to VM1 revealed that it is dominated by the components composing the second, actin-associated cluster of growth cone parameters identified in the correlation matrix—static and dynamic actin coherence (FIC and JSD) and the offset between the positions of the actin maximum and the projection maximum (Figure 7D; compare Figure 6C). Note that this is the cluster of parameters that is also consistently linked to instantaneous growth cone velocity (Figure 6C). These data demonstrate unambiguously that actin organization, and its connection to growth cone advance, is the overwhelming target of Abl. Since the PCA employs a normalized metric for variance, we can infer quantitatively that Abl has relatively little impact on the branching properties of the growth cone, while the magnitude of the variance Abl introduces in actin structure is ~10× as great as the variance separating the two morphological forms of TSM1. This is also supported by the Z-score for the effects of Abl on each of the 10 growth cone parameters, which reveals much greater effects on actin-associated parameters than on morphological features (Supplemental Figure S8).

DISCUSSION

What features define an axonal growth cone, and how do signaling molecules control its morphology and motility? Here we employed high-resolution live imaging of an axon developing in its native tissue to show that the TSM1 pioneer neuron of *Drosophila* has an almost purely filopodial morphology and that it employs a protrusive mode of growth as it extends. Quantitative analyses reveal two clusters of interlinked properties that define the morphology and dynamics of this growth cone. Multiple morphological parameters of the growth cone are strongly correlated and constrain it to exist in one of two interconvertible morphs that are closely related and that differ modestly in the complexity of their branching. This cluster of features, however, is largely insensitive to Abl, the conserved mediator of signaling from most of the characterized families of axon guidance receptors, and it does not show significant correlation to measures of growth cone advance. The second cluster, in contrast, comprised measures of actin organization and the spatial offset between the positions of the peaks of actin accumulation and filopodial distribution. This cluster is profoundly sensitive to Abl, and via the offset parameter, is consistently correlated with the instantaneous velocity of the growth cone. This provides compelling evidence that actin organization, and its relationship to the spatial localization of filopodial dynamics, is the critical target of guidance signaling in the growth cone.

The key challenge underlying analysis of axon growth and guidance has been to dissect how the advance of the protrusive, filopodial domain of the distal axon is achieved and directed. What is the target of the signaling machinery that acts downstream of guidance receptors? Is it morphology per se, or actin organization and dynamics, or some combination of both? To solve this problem, we developed a system for imaging the axon and its actin cytoskeleton, identified a set of quantifiable parameters that capture the properties of the growing axon, and reveal how those features are modi-

fied by the core cytoplasmic signaling machinery that regulates TSM1 development. Systematic, quantitative analysis of these data, in turn, then allowed us to infer the critical functions of guidance cue-dependent signaling in TSM1.

In the past, high-resolution analysis of axon growth has relied largely on imaging anonymous axons in culture (Lebrand *et al.*, 2004; Geraldo and Gordon-Weeks, 2009). This has the disadvantage, however, that cells lack the variety of growth and guidance cues found in vivo. Moreover, motility on rigid, relatively adherent substrata is known to be qualitatively different from motility in compliant, 3D media like that of most intact tissue (Cukierman *et al.*, 2001; Lammermann *et al.*, 2008; Liu *et al.*, 2015). In the current work, we image TSM1 as it extends in its native environment, the developing *Drosophila* wing. What we observed immediately is that the growing axon is almost purely filopodial in structure, and that it advances by selective stabilization of specific protrusions and disassembly of all others. Large lamellipodia are almost never observed in the leading portion of the axon (<1% of time points). Examination of published data from live imaging in vivo reveals that filopodial-dominated growth cones are observed commonly among pioneers in intact tissue (O'Connor and Bentley, 1993; Murray *et al.*, 1998; Leung and Holt, 2012; Sainath and Granato, 2013). Similarly, even in vitro, growth in compliant, 3D media produces a profound change in growth cone morphology, particularly the loss of the expanded leading lamella characteristic of adhesive motility (Ren and Suter, 2016). The profound difference in morphology and properties between this protrusive mode of growth and the more commonly studied adhesive growth on rigid substrata in vitro suggested that the underlying molecular mechanism of motility was apt to be equally different.

We next reasoned that interrogating the mechanism of axon growth and guidance required that we systematically modulate the core, guidance cue-dependent signaling machinery of the growth cone. Abl tyrosine kinase provides a uniquely powerful lever for achieving this. The Abl network transduces guidance signaling from many, if not most, of the common, phylogenetically conserved families of axon guidance receptors, such as the receptors for Netrin, Slit, Ephrins, Semaphorins, and others (Wills *et al.*, 1999; Bashaw *et al.*, 2000; Yu *et al.*, 2001; Crowner *et al.*, 2003; Forsthoefel *et al.*, 2005; Dajas-Bailador *et al.*, 2008), and control experiments verified that Abl signaling is essential for TSM1 development. Moreover, Abl directly regulates established biochemical pathways that modulate most of the elementary processes of actin dynamics, including polymerization, capping, and bundling (through Ena/VASP) (Krause *et al.*, 2002; Gates *et al.*, 2007; Bilancia *et al.*, 2014); branching (through WAVE and Arp2/3) (Insall and Machesky, 2009; Kannan *et al.*, 2017); and severing (through Rac, a regulator of Lim kinase and cofilin) (Kannan *et al.*, 2017; Tong *et al.*, 2018). Together, these properties make Abl an ideal reagent for dissecting guidance signaling to the actin cytoskeleton in TSM1.

Applying these tools, a systematic investigation of TSM1 revealed the fundamental organizational principles of the TSM1 growth cone and the nature of its regulation by Abl. Analysis of single morphological and organizational parameters, not surprisingly, revealed that many features of the growth cone are modestly altered by Abl signaling but did not shed much light on growth cone mechanism. In contrast, examining the pattern of correlations among parameters, first in pairwise combinations and then globally, revealed the properties that define the essential morphology of a growth cone and separated them from the properties that control its motion in response to the signaling networks downstream of guidance cues.

First, we found that TSM1 can occupy either of two branching morphs that are rather similar but quantitatively distinguishable. These correspond to two, closely spaced clouds of values distributed along the VM2 axis in PCA space, an axis that is dominated by the same quartet of branching measures observed in the analysis of pairwise correlations. Most wild-type growth cones remained in one morph or the other, though three cells underwent discrete transitions between them and one cell apparently fluctuated between the two. Visually, one morph (VM2-low) appears to be more complex in its branching pattern, while the other (VM2-high) appears simpler. Despite the categorical distinction between the two morphs, however, we did not detect any obvious functional difference between them; for example, their growth rates were not significantly different, nor did they segregate into different anatomical portions of the path of TSM1. Moreover, while altering Abl activity modified somewhat the relative occupancy of the two growth cone morphs, it had little effect on the range of values assumed by individual time points and showed no significant correlation with growth cone advance.

The same correlation and PCA analyses also revealed a second interlinked cluster of parameters, these describing actin organization and its spatial relationship to the site of filopodial dynamics. Unlike the morphological cluster, however, the actin-associated cluster was profoundly sensitive to Abl; altering Abl activity expands by a factor of 10 the envelope of parameter values available to the growth cone along this axis (VM1). Moreover, the actin cluster—specifically the spatial offset between the positions of the actin and projection peaks—showed consistent correlations with the instantaneous velocity of the growth cone, again unlike the morphological parameters.

The picture that emerges for the growth cone is of a structure that has a basic envelope of forms available to it, where this envelope is an intrinsic feature dictated by the genetic structure of the neuron. The function of guidance cue-dependent signaling is to modulate the organization of the actin core within that growth cone, and the spatial relationship between that actin core and the regional localization of filopodial dynamics, to regulate growth cone advance. Just what are the detailed changes that Abl induces in actin organization and how they in turn produce directed extension of the axon is the topic of the accompanying paper (Clarke et al., 2020).

MATERIALS AND METHODS
Drosophila stocks
Neuralized-Gal4, *Abl* KD (*UAS-Abl-RNAi*), *Abl* OE (*UAS-Abl*), *UAS Dicer2*, and the *abl⁴* allele have been described previously (Song et al., 2010; Kannan et al., 2014, 2017). *UAS-lifeactGFP*, and *UAS-CD4+ tandem tomato* stocks were obtained from the Bloomington *Drosophila* stock center.

TSM1 axon growth and guidance phenotypes
White prepupae marked at the start of pupariation in each genotype were aged 7.5–8 h at 25°C. Aged pupae were dissected in fresh culture media (CM) composed of Schneider's *Drosophila* media (Life Technologies) supplemented with 10% fetal bovine serum (Life Technologies). Wings were removed and placed in a 35-mm MatTek glass bottom microwell petri dish ventral side down and a halved circular coverslip was placed on their dorsal surface. Discs were slightly compressed to immobilize and flatten the tissue. Inert, compressible clay was placed between the bottom interior surface of the MatTek dish and the top cover glass to prevent over compression of the wings and to adhere the top coverslip to the bottom of the culture chamber (Supplemental Figure S9). CM (5 ml) was added to the dish after the tissue was secured in position. To assay

terminal axonal phenotypes, wing discs were aged for ~16 h at 25°C and microscopy was performed on a Zeiss LSM 880 w/Airy scan confocal microscope using a 25×/0.8 NA water immersion objective. Non-wild-type TSM1 axons assumed one of four distinguishable phenotypes: no axon extended, axonal stall, guidance defect, or aberrant collateral branches. For simplicity, all non-wild-type phenotypes were scored as aberrant.

Pharmacology: Abl kinase inhibition by Imatinib mesylate
A 100-mg tablet of Imatinib (Novartis, obtained from the National Institutes of Health (NIH) Clinical Center Pharmacy) was dissolved in 20 ml of Schneider's *Drosophila* medium producing a 10-mM stock, and aliquots were stored at –20C. Five microliters of 10 mM Imatinib/Schneider's suspension were added to 4.995 ml of CM for a final experimental concentration of 10 μM. Five milliliters of fresh 10 μM Imatinib CM was added to wild-type wing discs mounted as described above. Cultures were aged and imaged as described above.

Growth cone time-lapse imaging
Wing discs for the control, Abl-KD, and Abl-OE conditions were prepared and mounted as described above for scoring aberrant end-stage phenotypes. Live imaging was performed immediately after mounting at 25°C using an inverted Zeiss Axio Observer Z1 confocal microscope fitted with a Yokogawa Spinning Disk module and a temperature-controlled stage. Z-stacks at 0.8 μm spacing were collected from individual TSM1 axons using a 63×/1.2 NA water immersion objective. Laser power was set at a minimal value to mitigate photodamage and ensure image intensities were not saturated. Note that deconvolution of image stacks was *not* performed, as we found that the filtering intrinsic to standard deconvolution algorithms is incompatible with analyses of the information structure of the actin distribution (described below).

Segmentation of the axon and quantification of growth cone parameters
Neuronal z-stacks were stereoscopically reconstructed in 4D (x, y, z, and time) using IMARIS (Bitplane, version 8.0.2) and segmented using the semiautomatic "filament tracer" function. The axonal backbone and protrusions of TSM1 were identified and traced using the membrane localized CD4+ tandem tomato signal; false positives were removed manually, and untraced protrusions were added manually. Tracings were exported as inventor files (.iv) and converted to the standard SWC file format using a MiPav plug-in. Morphological parameters extracted from these segmented images included the number of protrusions, length of each protrusion, position of individual protrusions along the axon, and average protrusion branch order, among others (for a full list of measured parameters, see Figure 4A). Note that when calculating the number or total length of projections at a given point along the axon shaft, we summed all of the higher-order projections that emerged from a primary branch and assigned them to the position of that primary branch. Note also that we did not include the position of the tip of the leading protrusion of the growth cone as a parameter in our analyses due to the massive variability of this measurement and its failure to correlate discernably with any other aspect of morphology or dynamics (Yolland et al., 2019).

Custom scripts in Mathematica software were written to identify computationally the position of highest filopodial density along the axon by using a sliding-window method to sum the length and number of protrusions within a 5-μm window that advanced 1 μm per step along the segmented axon. We varied window size from 1 to

10 µm and empirically found peak protrusion density assignment was insensitive to the size of the window (unpublished data). We then calculated the square root of the second moment about the peak of protrusion density to determine the length of the protrusive zone, both separately for the portions of the distribution leading and trailing the peak position and also globally. The separate leading and trailing measurements were most effective for identifying biologically relevant positions in the growth cone; the global square root (sqrt)(second moment) was used only as a parameter in the PCA due to statistical considerations.

Actin distribution measurements

SWC files from a complete trajectory of TSM1 growth and the corresponding 4D Z stacks, (x, y, z, and time) converted to Nikon image cytometry standard format in Imaris were loaded into two MiPav plug-ins, PluginDrosophilaCreatesSWC and PlugIn3DSWCStats to extract the actin distributions from each time point. Plug-in code is available in MiPav, but its function is described below.

In brief, image intensity is calculated by summing the actin intensity within sequential frustums that encompass the axon. First, the MiPav plug-in performs a background subtraction on each image. A 3D probability map of intensity values is then generated to determine the boundaries of the actin signal. A circle is then expanded from each coordinate in the SWC tracing to determine the radius of each frustum. The radius is normal to the SWC axis and is bounded by the background of the image in the probability map. Summed intensity values from nonoverlapping frustums are then reported as a function of position along the axonal tracing. Actin maximum position was identified by sliding window and the square root of the second moment of the distribution was calculated just as for the equivalent measurements of filopodial density. The sqrt of the second moment of the actin distribution, measured relative to the global actin maximum, was selected empirically as the optimal definition for the boundaries of the "actin peak" for three reasons. First, the sqrt(second moment) corresponds well with growth cone morphology. In the subset of images where the limits of the growth cone were discernable by visual inspection, the boundaries of the sqrt(second moment) of the actin aligned well with the apparent morphological limits of the growth cone. Second, the sqrt(second moment) encompasses the actin peak. On aligning all the wild-type actin profiles by their respective global peak positions, averaging actin intensity across the data set and comparing the resulting curve with the positions of the average leading and trailing sqrt of the second moment, the sqrt(second moment) robustly spans the axonal region occupied by most of the actin distribution (Figure 3, A and B). Third, the sqrt(second moment) reliably predicts the limits of actin motion during growth. In 77% of individual time steps, the position of the actin peak fluctuates within the window defined by ± the sqrt of the second moment for that time step. Note that, just as for the filopodial peak (above), the leading and trailing sqrt(second moment) were most useful for defining biologically relevant positions in the growth cone and their sum most useful as a measure of the length of the actin peak, but for statistical reasons, the global sqrt(second moment) was used for the PCA analysis.

While using the sqrt(second moment) as the definition of the actin peak was useful both operationally and as a measure that could be calculated objectively by an automated computational pipeline, alternate definitions of the actin peak, such as using the leading and trailing half max about the actin maximum, yielded qualitatively similar results. Those alternative metrics, however, were far less satisfactory than was use of the second moment to define the extent of the growth cone, as they required complex, ad hoc rules and subjective assessments by the observer to define fiducial positions of the growth cone.

Growth cone velocity

The growth cone velocity (also referred to as the instantaneous rate of axon extension and as the change in growth cone center per time step) was calculated by determining the arithmetic midpoint between the positions of the leading and trailing sqrt(second moment) of actin about the global peak (Figure 4B), measuring its translocation in the next time step, and dividing by the actual time between collection of those image stacks. Calculations of axon extension rate using other fiducial marks, such as the position of the maximum of actin, or of filopodia, gave essentially identical results (see accompanying paper, Supplemental Figure S2).

Growth cone volume

To calculate growth cone volume, we first identified the junction between the axon shaft and the growth cone. For reasons explained above, this was defined as the position of the trailing sqrt(second moment) of the actin distribution. We then calculated the volume enclosed by the convex hull defined by this anchor point and by the tips of all projections that arose from the axon distal to the point of the axon/growth cone junction.

FI

The degree of fragmentation (roughness) of the actin distribution derived from each individual image frame was quantified by the FI, which is a measure of the amount of information that can be specified by the shape of a distribution. The FI for each actin distribution profile was calculated according to the formula

$$\int dx \left(\frac{d\left(p(x)^{1/2} \right)}{dx} \right)^2$$

using the trapezoid approximation to the integral, where $p(x)$ is the distribution of actin intensity (x) values for each actin profile. The FI sums the fragmentation of the distribution across all spatial scales, from high-frequency noise to large-scale separation of intensity masses across tens of microns.

JSD

The JSD was used to quantify the divergence, or lack of concordance, between actin distributions at different time steps of any single trajectory. In other words, it quantifies how much the actin distribution has changed when comparing one time point to another. It is calculated according to the formula

$$\text{JSD}\left(p \parallel r \right) = \frac{1}{2} \sum_{n=1}^{n=N} \left[p_n \log_2 \left(\frac{2p_n}{p_n + r_n} \right) + r_n \log_2 \left(\frac{2r_n}{p_n + r_n} \right) \right]$$

where p and r are two probability distributions, that is, actin distributions. Here we use the square root of the JSD, which is a true metric (it satisfies the triangle inequality).

Significance value for pairwise correlations

Pairwise correlations of parameters were analyzed by Pearson r value and Kendall tau. Significance was determined based on Kendall tau, as assessed both by Benjamini-Hochberg FDR, with FDR < 5% considered significant, and by p value, with modified Bonferroni correction: to account for correlations among the parameters, calculated p values were divided by 0.011, with a corrected

p value < 0.05 accepted as significant. Since these two significance criteria sometimes gave discordant results and have different advantages and disadvantages, we noted that Pearson $r > 0.2$ (or < -0.2) was an effective cutoff at which *both* significance criteria were generally satisfied and therefore we used that value as the selection criterion to choose individual parameter correlations for further analysis.

PCA

PCA was performed by applying standard methods of principal component regression to the wild-type data set. Abl KD and Abl OE datapoints were then projected onto the wild-type parameter space. To simplify interpretation, after principal component regression, Varimax rotation (Kaiser, 1958; Abdi, 2003) was performed on the first two principal components to segregate component loadings. In brief, this rotates a PCA plane of interest to separate optimally the contributions of individual parameters to each of the two axes, while maintaining the distances between datapoints in the PCA space. It therefore simplifies the interpretation of which parameters are contributing to each axis of the PCA plot. To indicate that a given graph is displaying the rotated projection, we label the axes as "VM" rather than "PC." The rotation is calculated using the equation

$$u_{n,q} = \sum_{n'=1}^{L} R_{nn'} v_{n',q}, \ q = 1, 2, \cdots N_Q$$

and selecting R_{ij} to maximize

$$V = \sum_{n=1}^{L} \frac{1}{N_Q} \sum_{q=1}^{N_Q} \left(u_{n,q}^2 - u_{\text{ave},n}^2 \right)^2$$

where

$$u_{\text{ave},n} = \frac{1}{N_Q} \sum_{q=1}^{N_Q} u_{n,q}$$

and N_Q is the number of quantities used to defined the PCA axes, v_n is the nth PCA eigenvector (associated with the nth largest eigenvalue) defining the nth axis, and $v_{n,q}$ are the contribution of quantity q to PCA eigenvalue n.

Statistics and reproducibility

All statistical tests and their respective parameters that were performed in this manuscript are reported in the text and figure legends. Sample randomization was not relevant, as only genotype, and no relevant aspect of phenotype, was detectable by visual inspection at the stage of sample selection for dissection. In-focus samples were excluded only if the absolute intensity of fluorescent signal was too low for quantification, or if at the time of initiating imaging 1) there was no axon visible in the vicinity of the normal trajectory, or 2) the axon showed no evidence of dynamics (i.e., the cell seemed dead). Trajectories were terminated if the TSM1 growth cone went out of the plane of focus or fasciculated with the L3 nerve, or after 90 min of imaging. Blinding was not relevant as all analyses were done with a common computational pipeline. No formal power analysis was done to determine sample size prior to initiating experiment; retrospective leave-out analyses demonstrated that all observations were robust to final sample size.

Data and code availability

Numerical data for all figures are included in Supplemental Datasheet S1. MiPav plug-in code for extraction of actin intensity profiles has been incorporated and released in the publicly available NIH image analysis package MiPav. MATLAB and Mathematica scripts are available on the publicly accessible NIH website: https://data.ninds.nih.gov/EGiniger/clarke/index.html

REFERENCES

Abdi H (2003). Factor rotations in factor analyses. In: Encyclopedia of Social Sciences Research Methods, ed. M. Lewis-Beck and A. Bryman, Thousand Oaks, CA: Sage.

Bashaw GJ, Kidd T, Murray D, Pawson T, Goodman CS (2000). Repulsive axon guidance: Abelson and Enabled play opposing roles downstream of the roundabout receptor. Cell 101, 703–715.

Bilancia CG, Winkelman JD, Tsygankov D, Nowotarski SH, Sees JA, Comber K, Evans I, Lakhani V, Wood W, Elston TC, et al. (2014). Enabled negatively regulates diaphanous-driven actin dynamics in vitro and in vivo. Dev Cell 28, 394–408.

Blair SS, Palka J (1985). Axon guidance in cultured wing discs and disc fragments of Drosophila. Dev Biol 108, 411–419.

Clarke A, McQueen PG, Fang HY, Kannan R, Wang V, McCreedy E, Wincovitch S, Giniger E (2020). Abl signaling directs growth of a pioneer axon in Drosophila by shaping the intrinsic fluctuations of actin. Mol Biol Cell 31, XXX–XXX.

Crowner D, Le Gall M, Gates MA, Giniger E (2003). Notch steers Drosophila ISNb motor axons by regulating the Abl signaling pathway. Curr Biol 13, 967–972.

Cukierman E, Pankov R, Stevens DR, Yamada KM (2001). Taking cell-matrix adhesions to the third dimension. Science 294, 1708–1712.

Dajas-Bailador F, Jones EV, Whitmarsh AJ (2008). The JIP1 scaffold protein regulates axonal development in cortical neurons. Curr Biol 18, 221–226.

Dent EW, Gertler FB (2003). Cytoskeletal dynamics and transport in growth cone motility and axon guidance. Neuron 40, 209–227.

Forsthoefel DJ, Liebl EC, Kolodziej PA, Seeger MA (2005). The Abelson tyrosine kinase, the Trio GEF and enabled interact with the Netrin receptor frazzled in Drosophila. Development 132, 1983–1994.

Gates J, Mahaffey JP, Rogers SL, Emerson M, Rogers EM, Sottile SL, Van Vactor D, Gertler FB, Peifer M (2007). Enabled plays key roles in embryonic epithelial morphogenesis in Drosophila. Development 134, 2027–2039.

Geraldo S, Gordon-Weeks PR (2009). Cytoskeletal dynamics in growth-cone steering. J Cell Sci 122, 3595–3604.

Grabham PW, Reznik B, Goldberg DJ (2003). Microtubule and Rac 1-dependent F-actin in growth cones. J Cell Sci 116, 3739–3748.

Grevengoed EE, Fox DT, Gates J, Peifer M (2003). Balancing different types of actin polymerization at distinct sites: roles for Abelson kinase and Enabled. J Cell Biol 163, 1267–1279.

Grevengoed EE, Loureiro JJ, Jesse TL, Peifer M (2001). Abelson kinase regulates epithelial morphogenesis in Drosophila. J Cell Biol 155, 1185–1198.

Insall RH, Machesky LM (2009). Actin dynamics at the leading edge: from simple machinery to complex networks. Dev Cell 17, 310–322.

Kaiser HF (1958). The varimax criterion for analytic rotation in factor-analysis. Psychometrika 23, 187–200.

Kannan R, Kuzina I, Wincovitch S, Nowotarski SH, Giniger E (2014). The Abl/enabled signaling pathway regulates Golgi architecture in Drosophila photoreceptor neurons. Mol Biol Cell 25, 2993–3005.

Kannan R, Song JK, Karpova T, Clarke A, Shivalkar M, Wang B, Kotlyans-kaya L, Kuzina I, Gu Q, Giniger E (2017). The Abl pathway bifurcates to balance Enabled and Rac signaling in axon patterning in Drosophila. Development 144, 487–498.

Koleske AJ, Gifford AM, Scott ML, Nee M, Bronson RT, Miczek KA, Baltimore D (1998). Essential roles for the Abl and Arg tyrosine kinases in neurulation. Neuron 21, 1259–1272.

Krause M, Bear JE, Loureiro JJ, Gertler FB (2002). The Ena/VASP enigma. J Cell Sci 115, 4721–4726.

Lammermann T, Bader BL, Monkley SJ, Worbs T, Wedlich-Soldner R, Hirsch K, Keller M, Forster R, Critchley DR, Fassler R, Sixt M (2008). Rapid leukocyte migration by integrin-independent flowing and squeezing. Nature 453, 51–55.

Lebrand C, Dent EW, Strasser GA, Lanier LM, Krause M, Svitkina TM, Borisy GG, Gertler FB (2004). Critical role of Ena/VASP proteins for filopodia formation in neurons and in function downstream of netrin-1. Neuron 42, 37–49.

Leung L, Holt CE (2012). Imaging axon pathfinding in Xenopus in vivo. Cold Spring Harb Protoc 2012, 984–991.

Lewis AK, Bridgman PC (1992). Nerve growth cone lamellipodia contain two populations of actin filaments that differ in organization and polarity. J Cell Biol 119, 1219–1243.

Liebl EC, Rowe RG, Forsthoefel DJ, Stammler AL, Schmidt ER, Turski M, Seeger MA (2003). Interactions between the secreted protein Amalgam, its transmembrane receptor Neurotactin and the Abelson tyrosine kinase affect axon pathfinding. Development 130, 3217–3226.

Lin CH, Forscher P (1995). Growth cone advance is inversely proportional to retrograde F-actin flow. Neuron 14, 763–771.

Liu YJ, Le Berre M, Lautenschlaeger F, Maiuri P, Callan-Jones A, Heuze M, Takaki T, Voituriez R, Piel M (2015). Confinement and low adhesion induce fast amoeboid migration of slow mesenchymal cells. Cell 160, 659–672.

Moresco EM, Koleske AJ (2003). Regulation of neuronal morphogenesis and synaptic function by Abl family kinases. Curr Opin Neurobiol 13, 535–544.

Murray MA, Schubiger M, Palka J (1984). Neuron differentiation and axon growth in the developing wing of Drosophila melanogaster. Dev Biol 104, 259–273.

Murray MJ, Merritt DJ, Brand AH, Whitington PM (1998). In vivo dynamics of axon pathfinding in the Drosophilia CNS: a time-lapse study of an identified motorneuron. J Neurobiol 37, 607–621.

O'Connor TP, Bentley D (1993). Accumulation of actin in subsets of pioneer growth cone filopodia in response to neural and epithelial guidance cues in situ. J Cell Biol 123, 935–948.

O'Connor TP, Duerr JS, Bentley D (1990). Pioneer growth cone steering decisions mediated by single filopodial contacts in situ. J Neurosci 10, 3935–3946.

Ren Y, Suter DM (2016). Increase in growth cone size correlates with decrease in neurite growth rate. Neural Plast 2016, 3497901.

Riedl J, Crevenna AH, Kessenbrock K, Yu JH, Neukirchen D, Bista M, Bradke F, Jenne D, Holak TA, Werb Z, et al. (2008). Lifeact: a versatile marker to visualize F-actin. Nat Methods 5, 605–607.

Sabry JH, O'Connor TP, Evans L, Toroian-Raymond A, Kirschner M, Bentley D (1991). Microtubule behavior during guidance of pioneer neuron growth cones in situ. J Cell Biol 115, 381–395.

Sainath R, Granato M (2013). Plexin A3 and turnout regulate motor axonal branch morphogenesis in zebrafish. PLoS One 8, e54071.

Song JK, Kannan R, Merdes G, Singh J, Mlodzik M, Giniger E (2010). Disabled is a bona fide component of the Abl signaling network. Development 137, 3719–3727.

Tong H, Qi D, Guan X, Jiang G, Liao Z, Zhang X, Chen P, Li N, Wu M (2018). c-Abl tyrosine kinase regulates neutrophil crawling behavior under fluid shear stress via Rac/PAK/LIMK/cofilin signaling axis. J Cell Biochem 119, 2806–2817.

Wills Z, Bateman J, Korey CA, Comer A, Van Vactor D (1999). The tyrosine kinase Abl and its substrate enabled collaborate with the receptor phosphatase Dlar to control motor axon guidance. Neuron 22, 301–312.

Yolland L, Burki M, Marcotti S, Luchici A, Kenny FN, Davis JR, Serna-Morales E, Muller J, Sixt M, Davidson A, et al. (2019). Persistent and polarized global actin flow is essential for directionality during cell migration. Nat Cell Biol 21, 1370–1381.

Yu HH, Zisch AH, Dodelet VC, Pasquale EB (2001). Multiple signaling interactions of Abl and Arg kinases with the EphB2 receptor. Oncogene 20, 3995–4006.